Science Bulletin 66 (2021) 1296–1304

Contents lists available at ScienceDirect

Science Bulletin

journal homepage: www.elsevier.com/locate/scib

Article

Efficient photoelectrochemical CO_2 conversion for selective acetic acid production

Xiaonong Wang [a,b,1], Chao Gao [a,1], Jingxiang Low [a,1], Keke Mao [c], Delong Duan [a], Shuangming Chen [a], Run Ye [a], Yunrui Qiu [a], Jun Ma [a], Xusheng Zheng [a], Ran Long [a,*], Xiaojun Wu [a], Li Song [a], Junfa Zhu [a], Yujie Xiong [a,b,*]

[a] Hefei National Laboratory for Physical Sciences at the Microscale, Collaborative Innovation Center of Chemistry for Energy Materials (iChEM), School of Chemistry and Materials Science, and National Synchrotron Radiation Laboratory, University of Science and Technology of China, Hefei 230026, China
[b] Institute of Energy, Hefei Comprehensive National Science Center, Hefei 230031, China
[c] School of Energy and Environment Science, Anhui University of Technology, Maanshan 243032, China

ARTICLE INFO

Article history:
Received 2 February 2021
Received in revised form 18 March 2021
Accepted 29 March 2021
Available online 6 April 2021

Keywords:
CO_2 reduction
Acetic acid
Photoelectrochemical
C_{2+} chemical
C–C coupling

ABSTRACT

Amidst the development of photoelectrochemical (PEC) CO_2 conversion toward practical application, the production of high-value chemicals beyond C_1 compounds under mild conditions is greatly desired yet challenging. Here, through rational PEC device design by combining Au-loaded and N-doped TiO_2 plate nanoarray photoanode with Zn-doped Cu_2O dark cathode, efficient conversion of CO_2 to CH_3COOH has been achieved with an outstanding Faradaic efficiency up to 58.1% (91.5% carbon selectivity) at 0.5 V vs. Ag/AgCl. Temperature programmed desorption and *in situ* Raman spectra reveal that the Zn-dopant in Cu_2O plays multiple roles in selective catalytic CO_2 conversion, including local electronic structure manipulation and active site modification, which together promote the formation of intermediate $^*CH_2$/$^*CH_3$ for C–C coupling. Apart from that, it is also unveiled that the sufficient electron density provided by the Au-loaded and N-doped TiO_2 plate nanoarray photoanode plays an equally important role by initiating multi-electron CO_2 reduction. This work provides fresh insights into the PEC system design to reach the multi-electron reduction reaction and facilitate the C–C coupling reaction toward high-value multicarbon (C_{2+}) chemical production via CO_2 conversion.

1. Introduction

The excessive CO_2 emission caused by overdependence on fossil fuels has led to a growing global climate anomaly, which is endangering the ecological balance. Direct conversion of CO_2 into storable value-added chemicals is an attractive and promising approach to realize a sustainable carbon cycle, and thus address the aggravating energy crisis and environmental issue [1,2]. In this regard, realizing efficient conversion of CO_2 under mild conditions through electrocatalysis or photocatalysis has been attracted ample attention from the scientific community [3,4]. Although the electrocatalytic and photocatalytic CO_2 conversion have been on the fast-track of development in the past several decades, these two approaches are facing their limitations at the current stage. While the electrocatalytic approach heavily relies on electricity input, the CO_2 conversion efficiency and selectivity toward high-value C_{2+} hydrocarbon products remain undesirable for the photocatalysis.

Photoelectrochemical CO_2 conversion, combining the advantages of both electrocatalysis and photocatalysis, offers a promising avenue for boosting the CO_2 conversion efficiency and lowering the energy input [5–7]. Compared with electrocatalysis, the input renewable solar energy in the PEC process can not only reduce electricity consumption from an economic point of view, but also supply additional photogenerated electrons that may alter the reaction pathway and intermediate species [8,9]. Moreover, the PEC system can significantly facilitate the photogenerated electron–hole separation as well as utilize external voltage to compensate for the potential deficiency, thereby enhancing the CO_2 conversion efficiency in comparison with photocatalysis. Typically, a PEC system consists of a photoanode for photogeneration of

* Corresponding authors.
E-mail addresses: longran@ustc.edu.cn (R. Long), yjxiong@ustc.edu.cn (Y. Xiong).
[1] These authors contributed equally to this work.

https://doi.org/10.1016/j.scib.2021.04.004
2095-9273/

active electron–hole pairs and a dark cathode for accepting photogenerated electrons from the photoanode and initiating the CO_2 reduction reaction. Clearly, the major function of the photoanode is to harvest the light, where the higher the light-harvesting ability of the photoanode, the higher the photoconversion efficiency of the PEC system. In other words, the photoanode mainly contributes for determining the number and energy of photogenerated electrons supplied to CO_2 reduction in the PEC system. Therefore, various strategies such as plasmonic metal loading and impurity doping have been extensively proposed for eking out the light-harvesting ability of semiconductor as the photoanode.

For the dark cathode, its main role is to establish the surface reaction (i.e., CO_2 reduction) for the PEC system, holding the other key to the overall CO_2 reduction efficiency and selectivity. As a perfect candidate for the dark cathode, a material should own enormous active sites and moderate adsorption toward intermediate compounds for subsequent C_{2+} species generation. In this respect, Cu-based materials have shown enormous potential due to their easy-tuned surface properties for active site exposure and moderate binding energy toward intermediate compounds. Among various types of Cu materials, oxide-derived Cu catalysts have proven their unique properties for CO_2 reduction because they can suppress H_2 evolution and show good selectivity for carbonaceous products [10,11]. Yet, the main reaction products using the oxide-derived Cu catalysts are normally limited to C_1 compounds such as methane (CH_4) and carbon monoxide (CO), creating a dilemma for its industrial application. In fact, the surface reaction of the dark cathode is closely related to the local electronic structure of catalytic sites. From this perspective, tuning the local electronic structure of the oxide-derived Cu through heteroatom doping has been one of the most effective strategies for optimizing the performance of the dark cathode. Following this line of thought, zinc element, which owns unique features for activating CO_2 and stabilizing carbonaceous intermediate, is often employed for manipulating the electronic structure of catalysts toward CO_2 reduction and realizing the C–C coupling [12–14]. It should be pointed out that the PEC approach is different from the photovoltaic (PV)-driven electrolysis system combining the tandem solar cell and electrocatalytic CO_2 reduction. The photoanode design together with adjustable external voltage in the PEC system, which can liberally control the number and energy of photogenerated electrons, offers a versatile knob for tuning the efficiency and selectivity of CO_2 reduction on the dark cathode.

Herein, we report a well-designed PEC system for direct CO_2 conversion into acetic acid. The dark cathode is built by Zn-doped Cu_2O on Cu foam, while the photoanode is fabricated by N-doped TiO_2 plate nanoarray modified by plasmonic Au nanoparticles, which can induce surface plasmon for improving photocatalytic activity via resonant energy transfer (RET) process as long as the plasmonic band overlaps the light absorption spectrum of semiconductor. As anticipated, Zn-dopants in Cu_2O enable the modification of the local electronic structure of Cu active sites and the stabilization of intermediates for C–C coupling. Meanwhile, the photocurrents are well regulated by tuning the light absorption of TiO_2 plate nanoarray through N-doping and plasmonic Au loading. It is revealed that proper bias voltage, appropriate photocurrent and effective Zn-modified Cu active site are interdependent and indispensable to achieve selective C–C coupling. With the optimization of the synergistic interplay among these aspects in the PEC system, highly efficient and selective conversion of CO_2 to CH_3COOH has been achieved with an outstanding Faradaic efficiency (FE) of up to 58.1% and a carbon selectivity of 91.5%. Interestingly, such a great achievement can be also realized using PV cells to supply bias voltage for PEC reaction.

2. Materials and methods

2.1. Materials and reagents

Tetraisopropyl titanate, hydrochloric acid (mass fraction 36.5%–38%), ammonium fluotitanate, zinc sulfate heptahydrate, copper sulfate pentahydrate, lactic acid, sodium hydroxide, ethanol and acetone were purchased from Sinopharm Chemical Reagent Co., Ltd. The water used in the experiments was deionized. All chemicals were used as received without further purification.

2.2. Preparation of TiO_2 and N-doped TiO_2 electrode

The TiO_2 plate nanoarrays were prepared using hydrothermal synthesis. Briefly, 10 mL of deionized water was mixed with 10 mL of concentrated hydrochloric acid (mass fraction 36.5%–38%) and stirred under ambient conditions for 5 min. Then 0.4 mL of tetrabutyl titanate was added and stirred for 15 min. 0.4 g ammonium fluotitanate was added into the solution and stirred for another 15 min to ensure the powder dissolving. The mixture was placed in a Teflon-lined stainless steel autoclave of 50 mL volume. Then one piece of fluorine-doped tin oxide (FTO) substrate (1×3 cm^2) was ultrasonically cleaned in acetone, ethanol and deionized water, and placed at an angle against the wall of the Teflon-liner. The hydrothermal synthesis was conducted at 170 °C for 12 h in an electric oven. After the synthesis, the FTO substrate was rinsed carefully with deionized water and dried in ambient air. The anatase TiO_2 plate nanoarrays were prepared by annealing in air at 450 °C for 2 h in a tube furnace, with a heating rate of 5 °C min^{-1}. As for N-doped TiO_2 plate nanoarrays, the sample was annealed in NH_3 at 450 °C for 2 h, with a heating rate of 2 °C min^{-1}.

2.3. Preparation of Au/N-doped TiO_2 electrode

The 4 nm Au film layer was deposited by using an ultrahigh vacuum (UHV) electron-beam evaporation system (DZS-500, Shenyang Scientific Instruments, China) on TiO_2 plate nanoarrays and N-doped TiO_2 plate nanoarrays. The evaporation rate was maintained at 0.01 nm s^{-1} under the pressure of about 10^{-4} mbar (1 mbar = 100 Pa).

2.4. Preparation of Zn-doped Cu_2O electrode

The Zn-doped Cu_2O electrode was prepared using electrodeposition. A three-electrode system was used to deposit Zn-doped Cu_2O on the Cu foam, with a platinum foil as the counter electrode, Ag/AgCl electrode as the reference electrode, and Cu foam (1 cm^2) as the working electrode. The electrolyte included 0.16 mol L^{-1} $ZnSO_4{\cdot}7H_2O$, 0.3 mol L^{-1} $CuSO_4{\cdot}5H_2O$ and 4 mol L^{-1} lactic acid. The temperature was set to 60 °C and the pH was adjusted by the addition of 4 mol L^{-1} sodium hydroxide. A constant applied potential of –0.38 V was employed for the working electrode by electrochemical workstation CHI 660D. The Zn contents in the final Zn-doped Cu_2O were regulated by adjusting the concentration of the $ZnSO_4{\cdot}7H_2O$ precursor. The concentrations of elements were measured with a Thermo Scientific PlasmaQuad 3 inductively-coupled plasma mass spectrometry (ICP-MS).

2.5. Characterizations

Scanning electron microscopy (SEM) images and energy-dispersive X-ray spectra (EDS) were taken on an FEI Sirion 200 field-emission scanning electron microscope operated at 5 kV. X-ray powder diffraction (XRD) patterns were recorded on a

Philips X'Pert Pro Super diffractometer with Cu Kα radiation (λ = 1.54178 Å). UV–vis diffuse reflectance data were recorded with a Shimadzu SolidSpec-3700 spectrophotometer. The liquid products were determined by nuclear magnetic resonance (NMR) spectroscopy (Bruker AVANCE AV III 400), in which 0.5 mL electrolyte was mixed with 0.1 mL D_2O (deuterated water) with 0.02 μL dimethyl sulfoxide (DMSO) as the internal standard. *In situ* Raman spectroscopy was performed with the Raman microscopy system (WITEC alpha300 R confocal Raman system) using 633 nm He–Ne laser as the excitation source during PEC CO_2 reduction. The Raman emission was collected by an Olympus 10× objective. Each presented spectrum is an average of five continuously acquired spectra with a collection time of 1 s each. The temperature-programmed desorption (TPD) profile of CO_2 was recorded on a Micromeritics AutoChem II 2920 chemisorption instrument. Prior to the adsorption of CO_2, the catalyst sample was pretreated at 200 °C for 1 h under He. After cooling to room temperature, the catalyst was saturated with CO_2 for 1 h. Then the catalyst was purged by He for 30 min and the TPD experiment started with a heating rate of 10 °C min^{-1}. The desorbed CO_2 was detected by a mass spectrometer. The positron annihilation lifetime (PAL) spectroscopy experiments were carried out with a digital PAL measurement system (TechnoAP) with a time resolution of ~200 ps. A 22Na source of 30 μCi was sandwiched between two identical samples, and the total count was 3 million. All the spectra were analyzed by the LIFETIME9 program. X-ray absorption fine structure (XAFS) characterization was performed at the beamline 1W1B of Beijing Synchrotron Radiation Facility (BSRF) and beamline BL14W1 of the Shanghai Synchrotron Radiation Facility (SSRF), China. The acquired extended XAFS (EXAFS) data were processed using the Demeter package (Athena for XAFS data preprocessing and Artemis for EXAFS data fitting). The structural parameters were selected using the given Zn/Cu_2O crystal model and the standard model of Cu_2O and Cu foil.

2.6. Photoelectrochemical measurements

The measurements were carried out on a CHI 660D electrochemical station (Shanghai Chenhua, China) in ambient conditions under irradiation of a 300-W Xe lamp (Solaredge 700, China). UV, visible or full-spectrum lights were used as the illumination source in the presence or absence of a 400 nm cutoff filter (short-wave-pass or long-wave-pass). The power densities of UV and visible light were measured to be 3 and 200 mW cm^{-2}, respectively. TiO_2, N-doped TiO_2 and Au/N-doped TiO_2 were used as the working electrode, Pt plate as the counter electrode, and the Ag/AgCl (filled with saturated KCl electrolyte) electrode as the reference electrode. The photoelectric responses (i.e., *I–t*, *I–V*) were operated by measuring the photocurrent densities under chopped light irradiation.

2.7. Photoelectrochemical CO_2 reduction

The photoelectrochemical CO_2 reduction tests were carried out in an H-type quartz reactor with the cathode and anode chambers separated by a Nafion film as the cation exchange membrane. Au/N-doped TiO_2 was used as the working electrode, Cu_2O or Zn-doped Cu_2O as the counter electrode, and the Ag/AgCl (filled with saturated KCl electrolyte) electrode as the reference electrode. The reactions were conducted in 0.5 mol L^{-1} Na_2SO_4 and 0.1 mol L^{-1} $KHCO_3$, respectively. The anode and cathode electrolytes were bubbling with Ar and pure CO_2 for 30 min before reaction, and the chambers were sealed during the reaction. The PEC reactions were carried out under 200 mW cm^{-2} illumination with a different voltage applied on the photoanode. Note that the Cu_2O typically exhibits poor photostability. To guarantee the long-term stability of our PEC system, the dark cathode was shielded from light irradiation during the reaction. The resultant gas products were measured by gas chromatography (GC, 7890A, Ar carrier, Agilent). H_2 was detected using a thermal conductivity detector (TCD). CH_4 was measured by a flame ionization detector (FID). CO was converted to CH_4 by a methanation reactor and then analyzed by the FID. The liquid products were determined by NMR (Bruker AVANCE AV III 400) spectroscopy. Solar cells were used to replace the electrochemical workstation to drive the reaction, with the photoanode connected to the positive electrode and the cathode connected to the negative electrode. The reaction was carried out through light illumination on both the solar cells and photoanode. The products were analyzed by GC and NMR.

3. Results and discussion

3.1. Structural characterization of electrodes

In this work, we aim for fabricating a PEC system with optimized photoanode and dark cathode to achieve highly efficient and selective CO_2 conversion toward high-value C_2 chemical production. We first obtain the dark cathode for such a system by electrodepositing Zn-doped Cu_2O with a Zn/Cu molar ratio of 0.015 (denoted as $Zn_{0.015}$-Cu_2O) onto the Cu foam. The morphology of the $Zn_{0.015}$-Cu_2O deposited on Cu foam is investigated via SEM images (Fig. 1a and b). As shown in Fig. 1a, the Cu foam substrate demonstrates a porous structure, providing enormous surface active sites for the later catalytic reaction. As revealed by the corresponding elemental mapping results, the Cu, O and Zn elements are homogeneously distributed on the sample, suggesting the successfully loading of $Zn_{0.015}$-Cu_2O onto the Cu foam. Such a Zn-doping does not alter the crystal phase of Cu_2O as confirmed by XRD (Fig. S1 online). In addition, according to Fig. 1b, the $Zn_{0.015}$-doped Cu_2O owns a pyramid shape and densely covers the surface of the Cu foam. Apart from $Zn_{0.015}$-doped Cu_2O, we also prepare a set of dark cathodes using Cu_2O and Zn-doped Cu_2O with a Zn/Cu molar ratio of 0.025 (denoted as $Zn_{0.025}$-doped Cu_2O) as comparison (Fig. S2 online). The chemical composition and elemental states of the prepared samples are further determined by X-ray photoelectron spectroscopy (XPS), showing the existence of Cu^{I} and Cu^{II} species (Fig. S3 online).

To attest the influence of Zn-doping on the local structure of Cu_2O, we collect PAL spectra for Cu_2O and Zn-doped Cu_2O (Fig. 1c) and calculate their corresponding lifetimes and relative intensities as shown in Table 1. Typically, the positrons could be trapped at defects such as vacancies, vacancy clusters and voids, thus reflecting the related surface information on the material. The PAL results for the prepared samples exhibit three distinct lifetime components including shorter lifetime (τ_1), longer lifetime (τ_2) and longest lifetime component (τ_3) with their corresponding percentage intensities, I_1, I_2 and I_3. Typically, τ_1 is associated with positron annihilation at the bulk or mono-vacancy defects, while τ_2 is assigned to positrons trapped by V_{Cu}^{-} – V_O^{+} vacancy complexes. The rest lifetime component τ_3 is attributed to the formation of *ortho*-positronium at the surface of micropores in the sample, which can always be elided due to its low contribution to the positron annihilation of semiconductor [15]. Our characterization shows lower I_1 and higher I_2 with the introduction of Zn content, indicating that Zn-dopant can promote the formation of V_{Cu}^{-} – V_O^{+} vacancy complexes.

The formation of V_{Cu}^{-} – V_O^{+} vacancy complexes is further affirmed by the synchrotron radiation-based XAFS spectroscopy. The normalized Cu K-edge X-ray absorption near-edge structure (XANES) spectra of $Zn_{0.015}$-doped Cu_2O in reference to pure Cu_2O (Fig. S4 online) demonstrate a slight shift of white line peak from 8995.13 eV (Cu_2O) to 8994.03 eV ($Zn_{0.015}$-doped Cu_2O), indicating

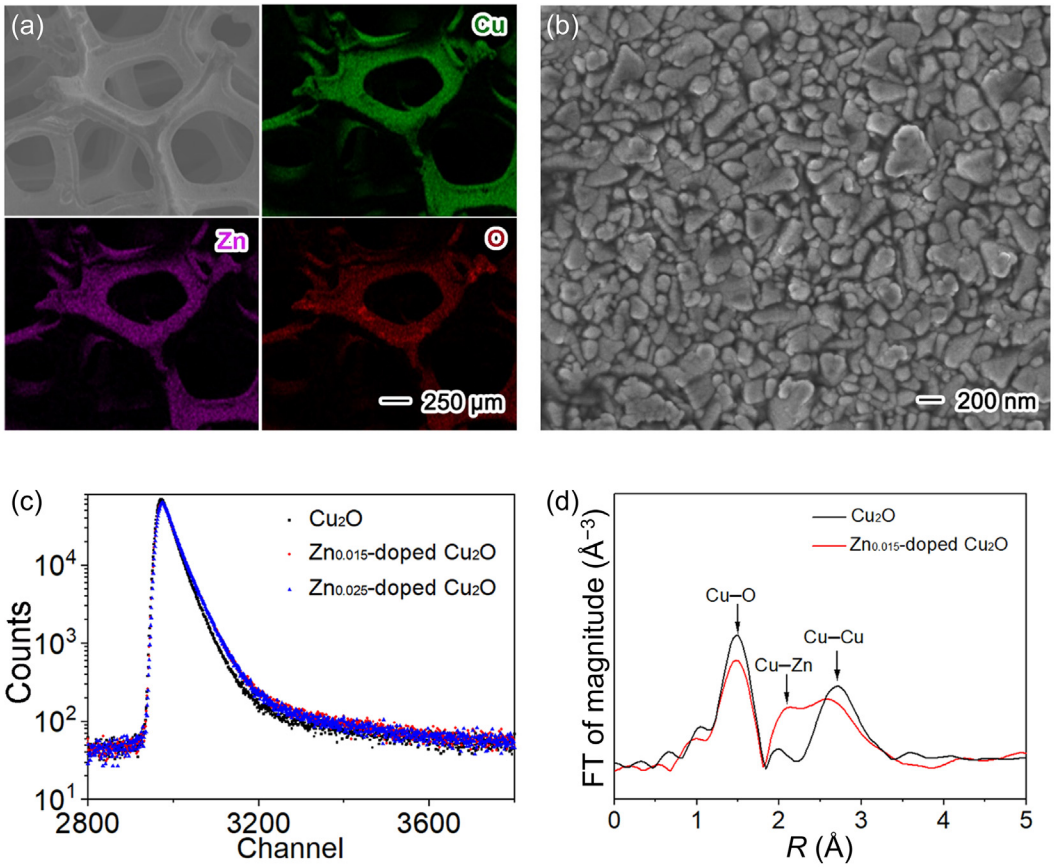

Fig. 1. Structural information of Zn-doped Cu_2O. (a) SEM images of $Zn_{0.015}$-doped Cu_2O on Cu foam, with the elemental mapping of Cu, Zn and O elements. (b) Magnified SEM image of $Zn_{0.015}$-doped Cu_2O on Cu foam. (c) Positron annihilation lifetime spectra of various samples (the channel width 10.4 ps). (d) The k^2-weighted Fourier-transform (FT) Cu K-edge EXAFS spectra for Cu_2O and $Zn_{0.015}$-doped Cu_2O, where R represents radial distance.

Table 1
The positron annihilation lifetimes and relative intensities of Cu_2O, $Zn_{0.015}$-doped Cu_2O and $Zn_{0.025}$-doped Cu_2O.

Sample	τ_1 (ps)	I_1 (%)	τ_2 (ps)	I_2 (%)	τ_3 (ps)	I_3 (%)
Cu_2O	183.4	46.23	322.0	52.03	2213	1.74
$Zn_{0.015}$-Cu_2O	171.2	26.52	349.5	70.73	2325	2.75
$Zn_{0.025}$-Cu_2O	169.2	30.46	353.4	66.94	2348	2.60

τ: Positron annihilation lifetime; I: Corresponding percentage intensities.

the lower oxidation state on $Zn_{0.015}$-Cu_2O. Furthermore, EXAFS spectra are processed through FT as shown in Fig. 1d. The peaks corresponding to the first-shell scattering path Cu–O and second-shell scattering path Cu–Cu of $Zn_{0.015}$-doped Cu_2O are less intense than those of Cu_2O, indicating the existence of oxygen vacancy and absence of some Cu atoms. In addition, the peak attributed to the second-shell scattering path Cu–Cu of $Zn_{0.015}$-doped Cu_2O (2.58 Å) shifts to a shorter bond length in comparison to that of Cu_2O (2.70 Å), due to the presence of Zn-dopant [16]. An additional peak at 2.12 Å ascribed to the Cu–Zn can be also observed, further confirming the successful doping of Zn into the Cu_2O lattice. To obtain the local bonding information for $Zn_{0.015}$-doped Cu_2O, EXAFS curve fitting analysis is performed as listed in Table S1 (online). For $Zn_{0.015}$-doped Cu_2O, coordination numbers (CNs) for Cu–O and Cu–Cu are calculated to be 1.44 and 11.12, respectively, which are significantly lower than those for Cu–O (2.0) and Cu–Cu (12.0) of Cu_2O. The decreases in CNs of $Zn_{0.015}$-doped Cu_2O further prove the presence of oxygen vacancy and absence of some Cu atoms, in good agreement with the results obtained from PAL in Table 1. The combination of Zn dopants with V_{Cu}^{-} – V_O^{+} vacancy complexes is anticipated to generate unique active sites for CO_2 reduction.

After gleaning the physicochemical information of the dark cathode, it is an essentially important task of rationally designing photoanode to enable broad light absorption and efficient electron–hole separation, which are two critical aspects for attaining high current density to provide effective and substantial energetic electrons for CO_2 conversion. Bearing this in mind, N-doped TiO_2 plate nanoarray with plasmonic Au nanoparticles confined (Au/N-doped TiO_2) is prepared on FTO substrate by hydrothermal and electron-beam evaporation methods (Figs. S5–S7 online). The successfully doping of N into TiO_2 enables sufficient overlap in the absorption spectrum of N-doped TiO_2 with that of the plasmonic Au (Fig. S8 online). As such, the RET process can directly enhance the electron–hole separation under light irradiation [17,18], substantially promoting photocurrent density. Such an Au/N-doped TiO_2 configuration provides an ideal photoanode for PEC CO_2 conversion.

3.2. PEC CO_2 conversion

After optimizing both the dark cathode and photoanode, we are now in a position to evaluate the performance of our designed PEC system (i.e., Au/N doped TiO_2 as the photoanode and $Zn_{0.015}$-doped Cu_2O as the dark cathode) for CO_2 conversion. Our designed Zn-doped Cu_2O cathode possesses the enhanced capability for CO_2 adsorption as Zn-doping can induce the formation of abundant CO_2 adsorption sites on Cu_2O (Fig. S9 online), forming the foundation for achieving excellent CO_2 reduction performance. We analyze the gas and liquid products from the PEC CO_2 conversion by gas chromatography, revealing that the main products are CH_3COOH with minor amounts of CO and H_2. Furthermore, ^1H NMR spectroscopy confirms that CH_3COOH is the only liquid product for CO_2 reduction and is indeed originated from CO_2 (Fig. S10 online) [19,20]. Such a monotony liquid product selectivity is beneficial for later product isolation during its practical application. We further compare the PEC CO_2 conversion performance of the different prepared dark cathodes at various applied bias potentials (Fig. 2a and Fig. S11 online). As indicated in Fig. 2a, the maximum FE for CH_3COOH reaches up to 58.1% with an applied bias potential at 0.5 V vs. Ag/AgCl using $Zn_{0.015}$-doped Cu_2O, while the FEs for CO and H_2 are only 5.2% and 5.9%, respectively, demonstrating a 91.5% carbon selectivity. Interestingly, the selectivity of the C_2 products heavily relies on the applied anodic potential. As the applied anodic potential becomes more negative or positive, the FEs for CH_3COOH significantly decrease. This result is because the lower bias voltage (<0.5 V vs. Ag/AgCl) can hardly drive the C–C coupling but just reduce Cu_2O or Zn-doped Cu_2O, while the higher bias voltage (>0.5 V vs. Ag/AgCl) can accelerate the amorphous carbon deposition, burying the catalytically active sites and inhibiting the production of multi-carbon compounds. In sharp contrast, when the bare Cu_2O and $Zn_{0.025}$-doped Cu_2O are used as the dark cathode, CO and H_2 are the main products with the absence of CH_3COOH irrespective of the applied bias potentials. These results clearly elucidate the effect of Zn-doping in promoting selective C–C coupling to produce CH_3COOH.

Since the ultimate goal in this work is to prepare efficient and simple-operated PEC devices for CO_2 conversion at an affordable cost, we introduce commercial Si solar cell, which harvests solar energy to generate electricity, for replacing the electrochemical station to supply bias voltage (see Fig. 2b and Fig. S12a (online) for the system configuration). In such a system, the light is shed on both photoanode and solar cell while dark cathode is shielded from the light. *I–V* curves of the solar cells illustrate that an output potential of 0.5, 1.0, 1.5, 2.0 and 3.0 V can be achieved (Fig. S12b online), corresponding to the 0.2, 0.4, 0.7, 1.2 and 2.0 V vs. Ag/AgCl reference electrode in this system, respectively. As shown in Fig. 2c, under full-spectrum sunlight illumination on the solar cell and the Au/N doped TiO_2 photoanode, the $Zn_{0.015}$-doped Cu_2O cathode produces 1.1 and 1.4 μmol CH_3COOH after 6 h of reaction with 1.0 and 1.5 V output potential, respectively. In contrast, with a lower voltage of 0.5 V or a higher voltage of 2 and 3 V, only CO and H_2 can be detected. Such an influence of the applied bias potentials is consistent with that using an electrochemical station. The success PEC CO_2 conversion driven by solar cell suggests that our designed PEC system can allow CO_2 conversion to be more flexible.

3.3. Reaction pathway and mechanism

Upon manifesting the CO_2 conversion performance, we intend to study the essential mechanism of how the fabricated PEC system

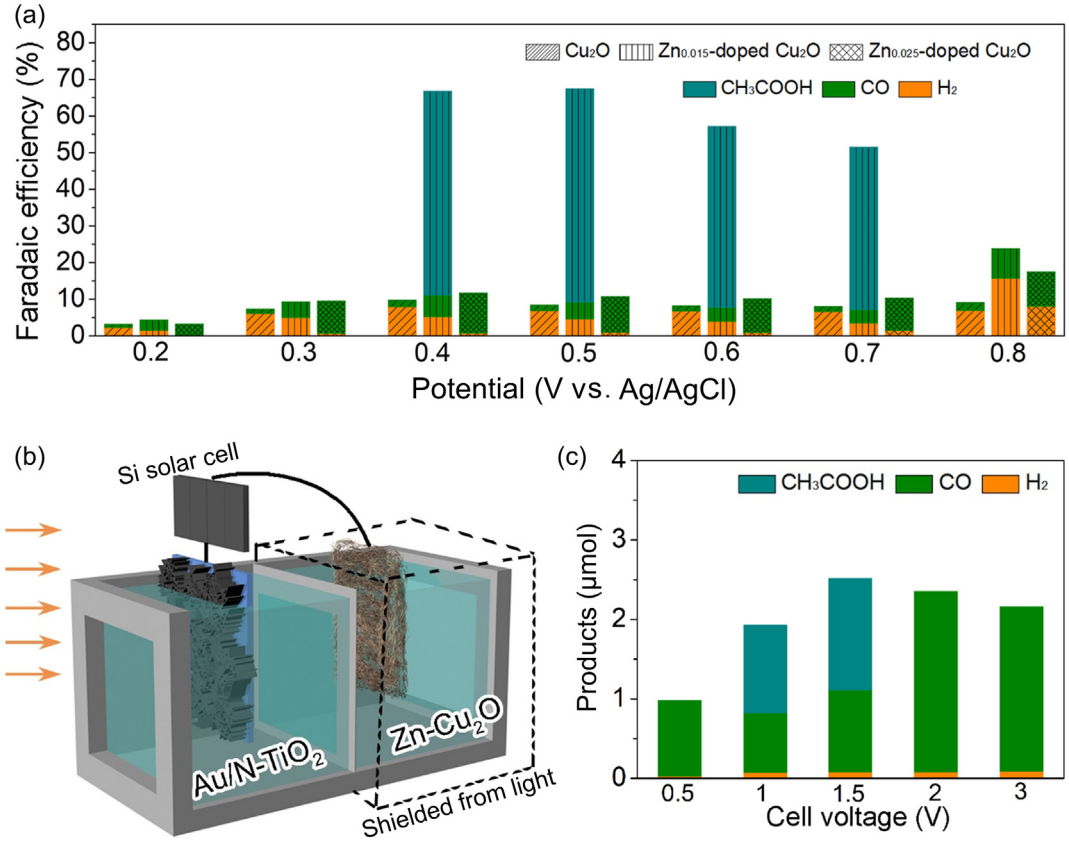

Fig. 2. PEC CO_2 conversion by different cathodes. (a) FE of products by Cu_2O, $Zn_{0.015}$-doped Cu_2O and $Zn_{0.025}$-doped Cu_2O, as the cathode, separately. (b) Schematic illustration for solar-cell-driven PEC system. (c) PEC CO_2 reduction products by $Zn_{0.015}$-doped Cu_2O in the solar-cell-driven system.

enables the production of CH_3COOH on $Zn_{0.015}$-doped Cu_2O. As described above, Zn-doping has altered the local structure of Cu_2O creating catalytically active sites for inducing C–C coupling in CO_2 conversion. To establish the correlation of C–C coupling with active sites, we have to decode the reaction pathways during the PEC CO_2 conversion. In this regard, *in situ* Raman spectra coupling electrochemical techniques can provide an efficient way to look into the "black box" of the reaction pathways on the Zn-doped Cu_2O for steering C–C coupling. Therefore, *in situ* Raman spectra for Cu_2O, $Zn_{0.015}$-doped Cu_2O and $Zn_{0.025}$-doped Cu_2O as a dark cathode and Au decorated N-doped TiO_2 as photoanode at the applied potential of 0.5 V vs. Ag/AgCl are recorded as shown in Fig. 3a–c. Generally, the peak at 525 cm^{-1} attributed to the Cu_2O can be observed at the beginning (0 min) [21]. After the introduction of CO_2 into the system, three new peaks arise at 703, 1064 and 1365 cm^{-1}, ascribed to C–O symmetric in-plane bending, C–O symmetric stretching and C–O anti-symmetric stretching of carbonate radical in H_2O, respectively [22,23]. With the evolution of reaction, three bands at 280, 350 and 2100 cm^{-1} ascribed to the restricted rotation of adsorbed CO (CO_{ads}), Cu–CO stretching mode and C–O stretching mode, respectively, appear and gradually increase (Fig. 3a–c) [22]. This reveals that *CO can be produced through all three systems.

Apart from the signals for *CO, additional peaks indicating C–C coupling can be observed on the $Zn_{0.015}$-doped Cu_2O with the evolution of reaction time. In detail, the bands at 1560 cm^{-1} for –COO stretching vibration, 2844 cm^{-1} for $*CH_2$ symmetric stretching, 2921 cm^{-1} for $*CH_3$ symmetric stretching and 1442 cm^{-1} for $*CO–*CH_2$ asymmetric deforming vibration gradually arise (see Fig. 3b and c) [24,25]. These results are consistent with the PEC CO_2 reduction results, where the CH_3COOH is the main product using $Zn_{0.015}$-doped Cu_2O as the dark cathode, while only CO and H_2 are produced using Cu_2O and $Zn_{0.025}$-doped Cu_2O as dark cathodes. Clearly, the introduction of appropriate Zn-dopant can significantly stabilize adsorbed CO and C–H intermediates, and thus change the reaction pathway of CO_2 conversion for C–C coupling.

To further elucidate the effect of Zn-doping on steering selective C–C coupling, the first principles simulation is employed to examine the adsorption behaviors of intermediates, the key to the formation of CH_3COOH, on Cu_2O and Zn-doped Cu_2O. In the simulation, the structural models for Cu_2O and $Zn_{0.015}$-doped Cu_2O (Fig. S13a and b online) are built according to the EXAFS results. The *in situ* Raman spectroscopy has revealed that the formation of $*CO–*CH_2$ is the key step for C–C coupling, toward which the formation and adsorption of two intermediates (*CO and $*CH_2$) constitute the pathway. As such, we first investigate the *CO adsorption configurations on Cu_2O and $Zn_{0.015}$-doped Cu_2O. It turns out that the most favorable *CO adsorption configurations take place on the top site of Cu adjacent to the two Zn sites for the $Zn_{0.015}$-doped Cu_2O (Fig. 3d), and on the top site of Cu for the Cu_2O (Fig. S12c online). As a result, the Zn-doping can substantially strengthen CO adsorption of Cu_2O from –0.451 to –0.951 eV, lowering the chance of CO desorption and thus enabling the *CO to take part in C–C coupling reaction. This fact is mainly responsible for the greatly suppressed CO production through Zn-doping.

The other key component for constituting $*CO–*CH_2$ is methylene ($*CH_2$) whose precursor should be formate (*OCHO). For this reason, the adsorption capabilities of Cu_2O and $Zn_{0.015}$-doped Cu_2O toward *OCHO are studied (see Fig. 3e and Fig. S13d online), showing the stronger adsorption on $Zn_{0.015}$-doped Cu_2O by the energy difference of 0.92 eV. This manifests that Zn-doping is beneficial for the adsorption and stabilization of *OCHO on the Cu_2O, allowing their subsequent transformation into C_2 products. In turn, the $*CH_2$ adsorption energies on the $Zn_{0.015}$-doped Cu_2O and Cu_2O are also calculated (see Fig. 3f and Fig. S13e online). The most favorable $*CH_2$ adsorption sites are on the bridge site of Zn–Zn for the $Zn_{0.015}$-doped Cu_2O, and on the bridge site of Cu–Cu for Cu_2O. Such a change in adsorption configuration leads to the significantly enhanced $*CH_2$ adsorption on $Zn_{0.015}$-doped Cu_2O by the energy difference of 1.15 eV. Taken together, the simulation demonstrates that the Zn-doping strengthens the adsorption of *CO, *OCHO and $*CH_2$ intermediates on Cu_2O, favoring the C–C coupling via the *CO insertion mechanism.

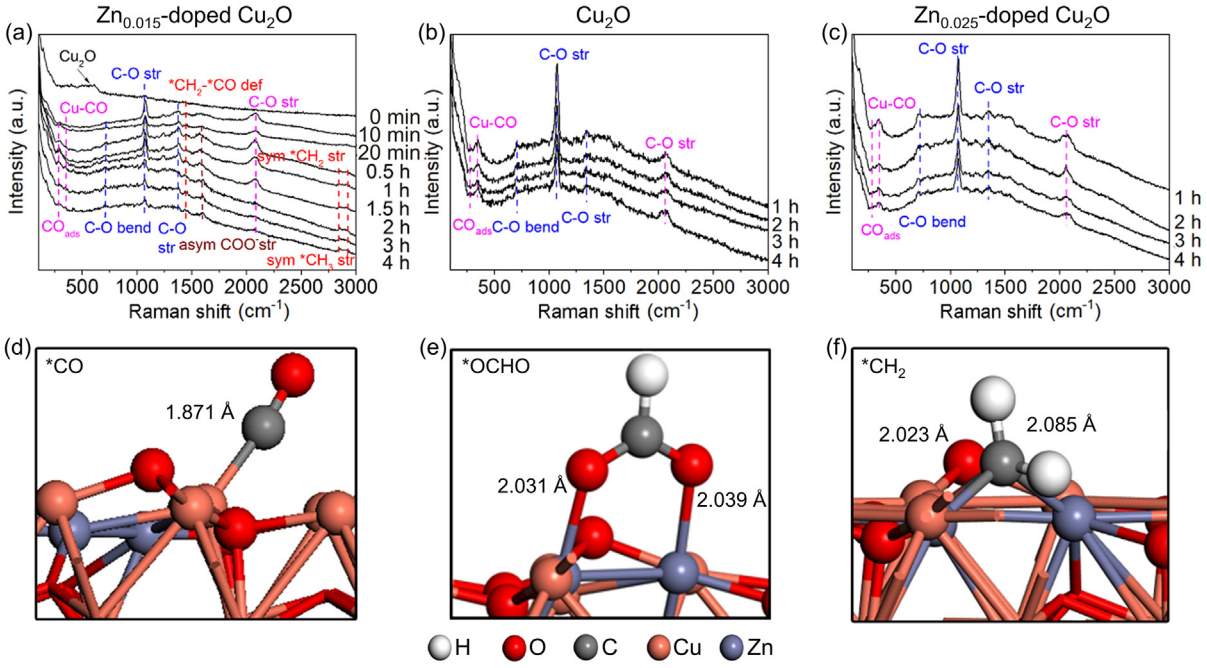

Fig. 3. *In situ* Raman spectroscopy and first-principles simulation for reaction. (a–c) *In situ* Raman spectra for PEC CO_2 conversion using $Zn_{0.015}$-doped Cu_2O (a), Cu_2O (b) and $Zn_{0.025}$-doped Cu_2O (c) at the applied potential of 0.5 V vs. Ag/AgCl. (d–f) The most favorable adsorption energies of *CO (d), *OCHO (e) and $*CH_2$ (f) on $Zn_{0.015}$-doped Cu_2O. All the results are obtained by first-principles simulations.

According to the above experimental and simulation results, the mechanism for enhanced PEC CO_2 conversion for C–C coupling over $Zn_{0.015}$-doped Cu_2O dark cathode can be proposed and shown in Fig. 4. During the PEC CO_2 reduction, the external voltage can enhance the separation efficiency of the photogenerated charge carriers on the Au/N-doped TiO_2 photoanode by guiding the photogenerated electron migration from photoanode to dark cathode of the PEC system for the reduction reaction [26]. The remaining holes on the photoanode can take part in the water oxidation and produce the protons, which subsequently migrate to the cathode through the proton membrane and contribute to the CO_2 conversion. After obtaining sufficient protons and electrons, CO_2 conversion reaction can be initiated on the $Zn_{0.015}$-doped Cu_2O dark cathode. Generally, the CO_2 can be first adsorbed on the $Zn_{0.015}$-doped Cu_2O via two intermediate species, including *OCHO and *COOH. For the *OCHO intermediate, it will undergo multi-step protons reduction to form $*OCH_2O$, and finally to $*CH_2$, which can be stabilized on the two adjacent Zn sites [27]. In the meantime, the *COOH intermediate can be easily transformed into the *CO and stabilized on the top Cu sites adjacent to the two Zn atoms. In turn, the $*CH_2$ and *CO intermediates tend to be coupled to form $*CO–*CH_2$ intermediate due to their adsorption on the neighboring sites on $Zn_{0.015}$-doped Cu_2O. Such a $*CO–*CH_2$ intermediate can be further reduced as the reaction further proceeds, finally selectively producing CH_3COOH on the $Zn_{0.015}$-doped Cu_2O.

3.4. Impact of photoanode and external voltage on PEC CO_2 conversion

It is worth mentioning again that the photoanode plays an equally important role in enhancing the CO_2 reduction performance of a PEC system. Typically, it determines the production of photogenerated electrons [28,29], which can dramatically manipulate the coverage of intermediate species and regulate the selectivity of products. In this respect, we perform the PEC CO_2 reduction using different photoanodes (Fig. 5a and b). When using the TiO_2, which exerts the lowest photocurrent, as the photoanode, only

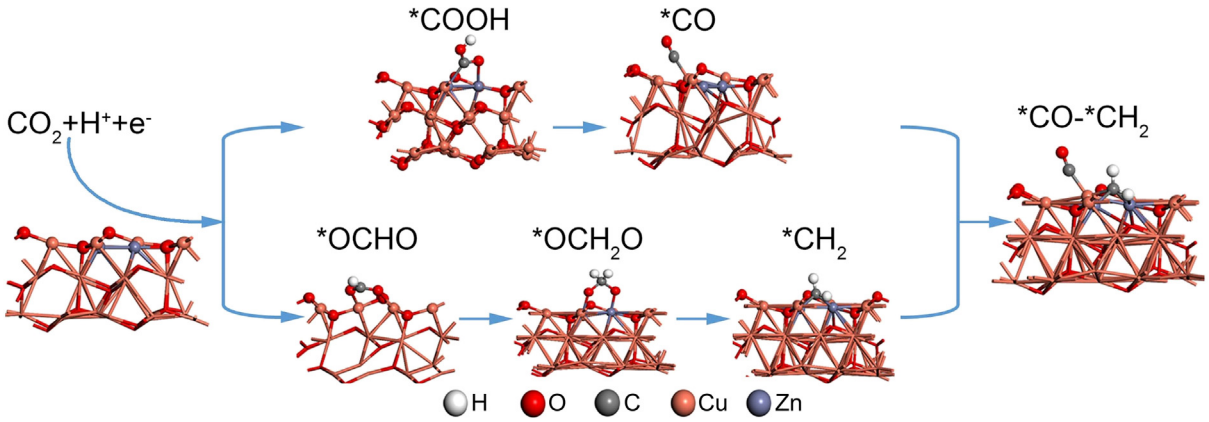

Fig. 4. Reaction pathway based on the *in situ* Raman spectroscopy and first-principles simulation.

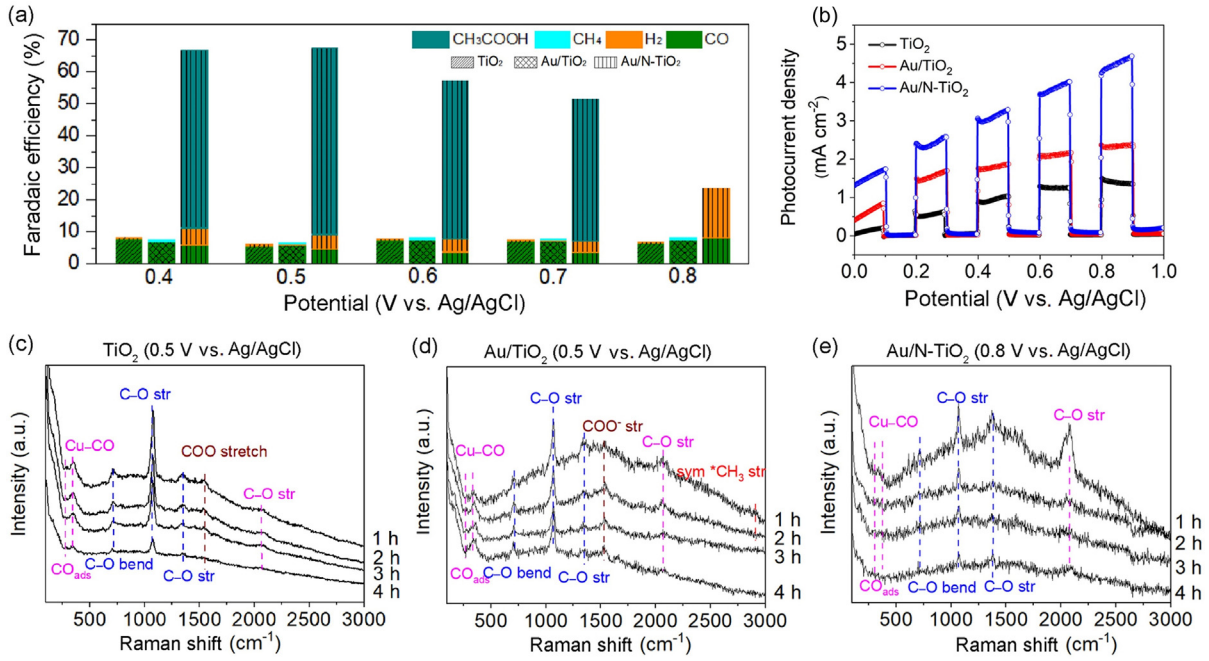

Fig. 5. Impact of photocurrents on the reaction pathway and product selectivity. (a) FE of products for PEC CO_2 conversion using TiO_2, Au/TiO_2 and Au/N-TiO_2 as the photoanode. (b) Photocurrent density for TiO_2, Au/TiO_2 and Au/N-TiO_2. (c–e) *In situ* Raman spectra for PEC CO_2 conversion using TiO_2 (c, 0.5 V vs. Ag/AgCl), Au/TiO_2 (d, 0.5 V vs. Ag/AgCl) and Au/N-TiO_2 (e, 0.8 V vs. Ag/AgCl).

two-electron products of CO and H_2 can be produced irrespective of the applied bias potential. After introducing the Au onto the TiO_2, the photocurrent density is 2 times enhanced, providing more photogenerated electrons for the CO_2 conversion. As a result, CH_4 can be obtained using Au/TiO_2 along with the production of CO and H_2. Yet, it can only generate a relatively low-value C_1 product. Interestingly, the formation of the C_2 product arises after increasing the photocurrent density by combining surface plasmon and N doping on the TiO_2. The increased electron density during the reaction can promote the formation and coverage of the intermediates (i.e., *OCHO, *COOH, *CO and *CH_2) on the dark cathode, thereby facilitating the C–C coupling to form CH_3COOH. As such, CH_3COOH turns out as the main product of the system with minor production of CO and H_2. The importance of the electron density can be further verified by altering the light intensity for the reaction (see Fig. S14 online). In details, when the lower light intensity (<200 mW cm^{-2}) is applied during the reaction, the photocurrent density is greatly reduced, resulting in negligible CH_3COOH production.

To comprehensively clarify the influence of photocurrent on the CO_2 conversion pathways, we perform the *in situ* Raman spectroscopic characterization using various photoanodes. Similar to the above results, all the samples show notable signals at 280, 350 and 2090 cm^{-1} attributed to *CO intermediates (Fig. 5c,d and Fig. 3a). When slightly enhancing photocurrents with Au/TiO_2 photoanode, an additional signal at 2900 cm^{-1} ascribed to C–H starts to show up (Fig. 5c). This indicates that high photocurrent helps form multi-electron –CH_x intermediates; however, their surface coverage is quite limited so that trace CH_4 is obtained in the final products. Once Au/N-TiO_2 is employed as photoanode, the signal at 2900 cm^{-1} for C–H is relatively strong (Fig. 3a) as the photocurrents are enhanced to a large extent. As a matter of fact, such a large-photocurrent system offers the high production selectivity for CH_3COOH. This demonstrates that the sufficiently high photocurrent is not only essential for producing active electrons for CO_2 reduction but also beneficial for increasing and stabilizing multi-electron –CH_x intermediates for achieving subsequent C–C coupling.

To further elucidate the influence of applied voltage on the PEC performance, we compare the *in situ* Raman spectrum of our PEC system performed at optimized applied bias voltage (0.5 V vs. Ag/AgCl, Fig. 3a) with that at lower bias voltage (0.2 V vs. Ag/AgCl, Fig. S15 online) and higher bias voltage (0.8 V vs. Ag/AgCl, Fig. 5e). Generally, both the lower and higher applied biases show only notable signals of adsorbed CO (CO_{ads}), Cu–CO stretching mode and C–O stretching mode, suggesting that the CO is their dominant product. More interestingly, although the signal at 2090 cm^{-1} attributed to *CO is greatly enhanced at the first 1 h of reaction after applying a relatively higher bias voltage of 0.8 V vs. Ag/AgCl, its signal gradually weakens with the evolution of reaction time due to the aforementioned amorphous carbon deposition problem. Taken together, the characterizations unambiguously reveal that a proper external bias voltage with a sufficiently high electron density on the photoanode is essential to attain multi-electron reduction products and avoid carbon deposition, and thus achieve efficient C–C coupling toward CH_3COOH production in our PEC system.

4. Conclusion

In conclusion, we have designed an efficient PEC system for direct CO_2 conversion to CH_3COOH with an outstanding FE of 58.1% and carbon selectivity of 91.5%. Such a superb performance has been achieved by rationally optimizing both the photoanode and dark cathode. Specifically, the Au-loaded and N-doped TiO_2 plate nanoarray is used as the photoanode for substantially enhancing the photocurrent density of the system, thus lowering power consumption and supplying sufficient electron density for multi-carbon production. For the dark cathode, the Zn-doped Cu_2O is employed with the aim of maximizing the surface active sites and tailoring the local structure of Cu_2O toward the promotion and stabilization of intermediates for achieving C–C coupling. It can be foreseen that such work on steering the C–C coupling can ignite future researches on C_{2+} hydrocarbon production through CO_2 conversion, thereby reaching its practical application in near future.

Conflict of interest

The authors declare that they have no conflict of interest.

Acknowledgments

This work was financially supported in part by the National Key R&D Program of China (2017YFA0207301, and 2017YFA0403402), the National Natural Science Foundation of China (21725102, 91961106, U1832156, 22075267, 21803002, 91963108, 21950410514, and U1732272), CAS Key Research Program of Frontier Sciences (QYZDB-SSW-SLH018), Science and Technological Fund of Anhui Province for Outstanding Youth (2008085 J05), Youth Innovation Promotion Association of CAS (2019444), Young Elite Scientist Sponsorship Program by CAST, China Postdoctoral Science Foundation (2019 M652190, 2020 T130627), Chinese Universities Scientific Fund (WK2060190096), MOST (2018YFA0208603) and DNL Cooperation Fund, CAS (DNL201922, DNL180201). XAFS measurements were performed at the beamline 1W1B of the Beijing Synchrotron Radiation Facility (BSRF) and beamline BL14W1 of the Shanghai Synchrotron Radiation Facility (SSRF), China. XPS experiments were performed at the photoemission end stations (BL10B) in National Synchrotron Radiation Laboratory (NSRL) in Hefei, China. We thank the support from USTC Center for Micro- and Nanoscale Research and Fabrication.

Author contributions

Yujie Xiong and Ran Long conceived the research and designed the experiments. Xiaonong Wang and Chao Gao carried out the experiments. Yunrui Qiu, Jun Ma and Xiaonong Wang contributed to photocatalytic performance measurement. Delong Duan, Shuangming Chen and Li Song contributed to the XAFS characterization. Run Ye contributed to the positron annihilation lifetime spectroscopy experiment. Xusheng Zheng and Junfa Zhu contributed to the XPS measurement. Keke Mao, Xiaojun Wu and Xiaonong Wang contributed to the DFT calculation. Xiaonong Wang, Chao Gao, Jingxiang Low, Ran Long and Yujie Xiong wrote the manuscript with input and comments from the other authors.

Appendix A. Supplementary materials

Supplementary materials to this article can be found online at https://doi.org/10.1016/j.scib.2021.04.004.

References

[1] Li F, Thevenon A, Rosas-Hernández A, et al. Molecular tuning of CO_2-to-ethylene conversion. Nature 2020;577:509–13.
[2] Lu Lu, Li Z, Chen Xi, et al. Spontaneous solar syngas production from CO_2 driven by energetically favorable wastewater microbial anodes. Joule 2020;4:2149–61.
[3] Chen C, Li Y, Yu S, et al. Cu-Ag tandem catalysts for high-rate CO_2 electrolysis toward multicarbons. Joule 2020;4:1688–99.

[4] Jiang Z, Xu X, Ma Y, et al. Filling metal-organic framework mesopores with TiO_2 for CO_2 photoreduction. Nature 2020;586:549–54.
[5] Andrei V, Reuillard B, Reisner E. Bias-free solar syngas production by integrating a molecular cobalt catalyst with perovskite-$BiVO_4$ tandems. Nat Mater 2020;19:189–94.
[6] Deng X, Li R, Wu S, et al. Metal-organic framework coating enhances the performance of Cu_2O in photoelectrochemical CO_2 reduction. J Am Chem Soc 2019;141:10924–9.
[7] Liu D, Liu B. Novel design of photoelectrochemical device by dual $BiVO_4$ photoelectrode with abundant oxygen vacancy. Sci Bull 2018;63:1027–8.
[8] Kang Y, Chen R, Zhen C, et al. An integrated thermoelectric-assisted photoelectrochemical system to boost water splitting. Sci Bull 2020;65:1163–9.
[9] Shen H, Gu Z, Zheng G. Pushing the activity of CO_2 electroreduction by system engineering. Sci Bull 2019;64:1805–16.
[10] Brito JF, Genovese C, Tavella F, et al. CO_2 reduction of hybrid Cu_2O-Cu/gas diffusion layer electrodes and their integration in a Cu-based photoelectrocatalytic cell. ChemSusChem 2019;12:4274–84.
[11] Chang X, Wang T, Zhao Z-J, et al. Tuning Cu/Cu_2O interfaces for the reduction of carbon dioxide to methanol in aqueous solutions. Angew Chem Int Ed 2018;57:15415–9.
[12] Zhao YT, Cui CN, Han JY, et al. Direct C-C coupling of CO_2 and the methyl group from CH_4 activation through facile insertion of CO_2 into Zn-CH_3 sigma-bond. J Am Chem Soc 2016;138:10191–8.
[13] Lee JK, Kim YJ, Choi Y-S, et al. Zn-containing ionic liquids bearing dialkylphosphate ligands for the coupling reactions of epoxides and CO_2. Appl Catal B 2012;111-112:621–7.
[14] Zhao Y, Wang H, Han J, et al. Active site ensembles enabled C-C coupling of CO_2 and CH_4 for acetone production. J Phys Chem C 2018;122:9570–7.
[15] Sellaiyan S, Vimala Devi L, Sako K, et al. Effect of dopant concentration and annealing of Yttrium doped CuO nanocrystallites studied by positron annihilation spectroscopy. J Alloy Compd 2019;788:549–58.
[16] Sankar G, Vasudevan S, Rao CNR. An EXAFS investigation of Cu-ZnO methanol Synthesis catalysis. J Chem Phys 1986;85:2291–9.
[17] Cushing SK, Li JT, Meng FK, et al. Photocatalytic activity enhanced by plasmonic resonant energy tansfer from metal to semiconductor. J Am Chem Soc 2012;134:15033–41.
[18] Li J, Cushing SK, Bright J, et al. Ag@Cu_2O core-shell nanoparticles as visible-light plasmonic photocatalysts. ACS Catal 2013;3:47–51.
[19] Sun S, Watanabe M, Wu Ji, et al. Ultrathin WO_3·$0.33H_2O$ nanotubes for CO_2 photoreduction to acetate with high selectivity. J Am Chem Soc 2018;140:6474–82.
[20] Hutchison MJ, Zhou P, Ogle K, et al. Enhanced electrochemical Cu release from commercial Cu-Sn alloys: fate of the alloying elements in artificial perspiration. Electrochim Acta 2017;241:73–88.
[21] Chan HYH, Takoudis CG, Weaver MJ. Electrochemical control of gas-phase oxidation and reduction of copper as probed by surface-enhanced Raman spectroscopy. Electrochem Solid St 1999;2:189–91.
[22] Akemann W, Otto A. Vibrational-modes of CO adsorbed on disordered copper-films. J Raman Spectrosc 1991;22:797–803.
[23] Tavender SM, Johnson SA, Balsom D, et al. The carbonate, Co_3^{-}1. solution studied by resonance Raman spectroscopy. Laser Chem 1999;19:311–6.
[24] Musumeci A, Frost RL. A spectroscopic and thermoanalytical study of the mineral hoganite. Spectrochim Acta A 2007;67:48–57.
[25] Socrates G. Infrared and Raman characteristic group frequencies: tables and charts. 3rd ed. London: John Wiley & Sons; 2004.
[26] Qiu Y, Pan Z, Chen H, et al. Current progress in developing metal oxide nanoarrays-based photoanodes for photoelectrochemical water splitting. Sci Bull 2019;64:1348–80.
[27] Duan X, Xu J, Wei Z, et al. Metal-free carbon materials for CO_2 electrochemical reduction. Adv Mater 2017;29:1701784.
[28] Chung HY, Chen W, Wen X, et al. Oxygen-deficient bismuth tungstate and bismuth oxide composite photoanode with improved photostability. Sci Bull 2018;63:990–6.
[29] Liu J, Dai M, Wu J, et al. Electrochemical hydrogenation of mixed-phase TiO_2 nanotube arrays enables remarkably enhanced photoelectrochemical water splitting performance. Sci Bull 2018;63:194–202.

Xiaonong Wang received her B.S. degree in Material Physics in 2011 from Northwestern Polytechnical University and Ph.D. degree in Inorganic Chemistry in 2018 from University of Science and Technology of China (USTC). She worked as a postdoctoral fellow at USTC from 2018 to 2020 and currently works as an associate professor at National University of Defense Technology, China. Her research interest focuses on photo and photo-electro catalysts design for CO_2 reduction.

Ran Long is an associate professor at the USTC. She received her Ph.D. degree in Inorganic Chemistry under the tutelage of Professor Yujie Xiong in 2014, from the USTC. Her research interest focuses on controlled synthesis and catalytic applications of metal nanocrystals.

Yujie Xiong is the Cheung Kong Chair Professor of Chemistry at the USTC. He received his Ph.D. degree in Inorganic Chemistry in 2004 from the USTC. His research centers on solar-driven artificial carbon cycle.